

Tunable quadruple-well ferroelectric van der Waals crystals

John A. Brehm^{1,2,7}, Sabine M. Neumayer^{1,3,7}, Lei Tao^{1,4,7}, Andrew O'Hara¹, Marius Chyasnavichus³, Michael A. Susner⁵, Michael A. McGuire², Sergei V. Kalinin^{1,3}, Stephen Jesse³, Panchapakesan Ganesh^{1,3}, Sokrates T. Pantelides^{1,2,6*}, Petro Maksymovych^{1,3*} and Nina Balke^{1,3*}

The family of layered thio- and seleno-phosphates has gained attention as potential control dielectrics for the rapidly growing family of two-dimensional and quasi-two-dimensional electronic materials. Here we report a combination of density functional theory calculations, quantum molecular dynamics simulations and variable-temperature, -pressure and -bias piezoresponse force microscopy data to predict and verify the existence of an unusual ferroelectric property—a uniaxial quadruple potential well for Cu displacements—enabled by the van der Waals gap in copper indium thiophosphate (CuInP₂S₆). The calculated potential energy landscape for Cu displacements is strongly influenced by strain, accounting for the origin of the negative piezoelectric coefficient and rendering CuInP₂S₆ a rare example of a uniaxial multi-well ferroelectric. Experimental data verify the coexistence of four polarization states and explore the temperature-, pressure- and bias-dependent piezoelectric and ferroelectric properties, which are supported by bias-dependent molecular dynamics simulations. These phenomena offer new opportunities for both fundamental studies and applications in data storage and electronics.

Recently, the family of layered thio- and seleno-phosphates has gained attention as potential control dielectrics for the rapidly growing family of two-dimensional (2D) and quasi-2D electronic materials¹. The relatively low oxidation states of metal ions stabilized in thiophosphates lead to a panoply of desired properties, including magnetic, dipolar and correlated electron orderings, providing new opportunities for functional van der Waals (vdW) heterostructures², electric field-tunable interfaces and layered materials with an intermediate optical band gap³. In particular, these materials open a straightforward path to ultra-thin ferroic structures through exfoliation, while avoiding the dangling bonds inevitable in materials with three-dimensional (3D) bonding. They enable electric field-tunable interfaces with 2D materials such as graphene and transition-metal dichalcogenides (TMDs) towards beyond-Moore electronic devices, including tunnel junctions and ferroelectric field-effect transistors. Furthermore, they exhibit substantial ionic conductivity^{4–6} that could lead to unexplored coupling phenomena, such as ferroionic states⁷. Common to all these perspectives is the fundamental question of the role of the vdW gap in the formation of the structurally, electronically and magnetically ordered states, and whether the vdW gap enables new ways to control these behaviours, complementary to or even unachievable in traditional materials with rigid lattices.

Bulk CuInP₂S₆ (CIPS), in particular, is ferroelectric^{8–12} wherein the Cu and In atoms displace in opposite directions within each layer⁹. For simplification purposes we will refer to CIPS as ferroelectric. Despite the low polarization values of about 3.5 $\mu\text{C cm}^{-2}$ close to room temperature^{9,12}, CIPS has recently been revealed to possess negative longitudinal piezoelectric coefficients^{8,13,14}. Negative longitudinal

piezoelectric coefficients are rare. Only one other material, poly(vinylidene fluoride), is known to have such a property experimentally demonstrated¹⁵. Theoretical studies of hexagonal ABC ferroelectrics¹⁶, other wurtzite and zinc-blende compounds^{17,18} and twinned ferroelectric perovskites with directed domain walls¹⁹ have predicted such an effect, but it has not been realized experimentally. At $T > \sim 42^\circ\text{C}$, Cu atoms are very mobile and can occupy both intra- and interlayer positions, leading to a disordered state^{9,11}. This finding was confirmed in a recent paper by You et al.¹⁸, who described two distinct phases with different polarization values. The piezoelectric or ferroelectric properties of the second, high-polarization, phase were not investigated.

Here, we report the discovery of an unusual ferroelectric property enabled by the vdW gap in CIPS, namely a uniaxial quadruple-potential well for Cu displacements. We theoretically and experimentally demonstrate the implications of this unusual property for fundamental properties such as polarization and piezoelectricity. We first report density functional theory (DFT)-based total-energy calculations as a function of continuous Cu displacements, revealing the existence of two energy minima in each polarization direction along the *z*-axis. The quadruple-well feature is directly enabled by the layered structure, which leads to a second stable Cu position within the vdW gap with only a small energy barrier between them. The evolution of the quadruple-well potential and the mechanical stress in the system as functions of applied strain are used to deduce the longitudinal piezoelectric constant of each of the two polar phases. Spatially resolved variable-temperature piezoelectric-force-microscopy (PFM) measurements were used to demonstrate gradual interconversion of the two phases as

¹Department of Physics and Astronomy, Vanderbilt University, Nashville, TN, USA. ²Materials Science and Technology Division, Oak Ridge National Laboratory, Oak Ridge, TN, USA. ³Center for Nanophase Materials Sciences, Oak Ridge National Laboratory, Oak Ridge, TN, USA. ⁴University of Chinese Academy of Sciences & Institute of Physics, Chinese Academy of Sciences, Beijing, China. ⁵Aerospace Systems Directorate, Air Force Research Laboratory, Wright-Patterson Air Force Base, OH, USA. ⁶Department of Electrical Engineering and Computer Science, Vanderbilt University, Nashville, TN, USA. ⁷These authors contributed equally: John A. Brehm, Sabine M. Neumayer, Lei Tao. *e-mail: pantelides@vanderbilt.edu; maksymovychp@ornl.gov; balken@ornl.gov

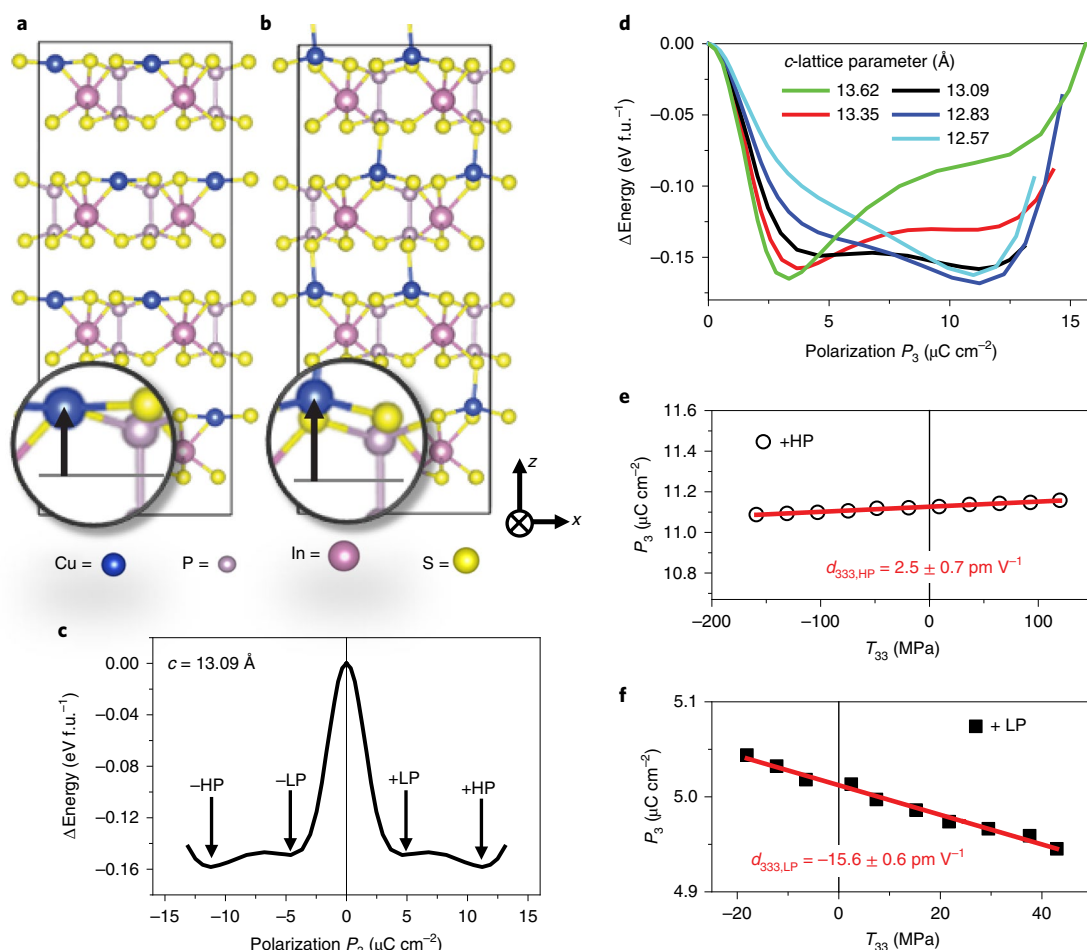


Fig. 1 | Quadruple well for CIPS and piezoelectric constant for polarization states obtained by DFT. **a**, For a *c*-lattice parameter of 13.09 Å, the relaxed structure of CIPS corresponding to the first local energy minimum described in the text. **b**, The relaxed structure of CIPS corresponding to the second local energy minimum (all structural images in this paper were created with the VESTA software package)³⁷. Insets in **a,b** show the start of *z*-position shift for Cu atoms. **c,d**, For lattice parameters of 13.09 Å (**c**) and 13.62, 13.35, 12.83 and 12.57 Å (**d**), change in energy versus the polarization extracted from the displacement of Cu per formula unit (f.u.). Each curve is the result of a total-energy calculation at a fixed strain-lattice parameter. The curves are plotted as functions of Cu displacement relative to zero displacement. **e,f**, Linear fit of the theoretical polarization versus stress (T_{33}) curves along the *z* direction around the zero-stress state for the +LP (**e**) and the +HP state (**f**). The relative ratio of the *x*- and *y*-axis ranges was kept constant for visual comparison of slopes.

the Curie temperature is approached. Finally, we report the ability to transform between polarization states through locally applied electric fields in experiment and theory. Overall, these findings establish the importance of chemical interactions across the vdW gap in this and possibly other layered solids. They further point to a deterministic pathway by which to increase spontaneous polarization in this family of materials.

Potential energy calculations for Cu

To examine the ferroelectric properties of CIPS, we investigated the potential energy surface of polar displacements, in this case Cu displacements, by means of DFT (see Methods). The relaxed monoclinic structure of CIPS is displayed in Fig. 1a. We performed a series of calculations using the found equilibrium lattice constant of 13.09 Å, placing the Cu atoms at the mid-plane of each layer and gradually displacing them to and beyond their equilibrium positions, as is standard practice in calculations for ferroelectrics, seeking to establish the displacement pathways and energy barriers for polarization switching. At each step of the calculations, Cu *z* displacement was kept fixed relative to the centre line by freezing the *z* coordinates of the Cu and one P atom per dipole, while all other

atoms were relaxed. Polarization values were then obtained via total Berry-phase calculations. Based on crystal symmetry, the polarization value along *y* is zero. It was found that the polarization values along *x* are one order of magnitude smaller compared to those along the *z* axis and can, therefore, be disregarded.

The potential energy drop (Fig. 1c) from the zero-displacement Cu site is comparable to results obtained by Song et al. for CuInP₂Se₆ (ref. 20). However, there is a second energy minimum when the Cu atom is occupying a stable position within the vdW gap forming interlayer bonds with S atoms from adjacent layers (Fig. 1b). It follows that there exist four local energy minima along the *z* axis, two in each of the polarization directions along *z*. The first local energy minimum is at a Cu-ion displacement of ~1.62 Å, which corresponds to polarization $P_3 = \pm 4.93 \mu\text{C cm}^{-2}$, close to the experimentally measured polarization^{9,12}. The second energy minimum is at a Cu-ion displacement of ~2.25 Å, which corresponds to $P_3 = \pm 11.26 \mu\text{C cm}^{-2}$, more than double the reported values when Cu is displaced into the vdW gap. In the following, we will refer to these states as low-polarization (LP) and high-polarization (HP) phases, respectively. Furthermore, we shall use the notation of a total of four polarization states, $\pm\text{LP}$ and $\pm\text{HP}$, with the sign

indicating their parallel or anti-parallel orientation with respect to the z axis. Based on terminology introduced by Stengel and Inguez²¹, we describe CIPS as a ferroelectric material with a quadruple-well potential curve as a function of Cu displacements along the c axis or polarization values, or simply quadruple-well ferroelectric, reflecting this meaning.

We note that the total-energy curve shown in Fig. 1c is calculated at a fixed c -lattice parameter (fixed volume), the equilibrium value of the LP phase, whereby the energy of the HP state would be lowered following relaxation of the c parameter. Indeed, as shown in Supplementary Fig. 1a, the relaxed structure of the HP phase has an equilibrium c -lattice parameter of 12.87 Å. We confirmed the existence of the quadruple-well potential for Cu displacement even under relaxing lattice parameters (Supplementary Fig. 2).

Unlike materials with independent double-well ferroelectric phases with different polarization axes that can be accessed by electric field (for example, BiFeO₃)²², the two CIPS phases cannot be described individually as normal double-well potential ferroelectric phases due to the uniaxial polarization vector of the LP and HP phases and the strong overlap of the total-energy curves. In particular, the pathway of Cu displacements between the +HP and –HP state contains the stable Cu positions of the LP phase, which generate additional local minima in the potential energy curve. Therefore, the terminology of a quadruple-well ferroelectric is more accurate than describing CIPS as a material with two distinct ferroelectric phases each characterized by a double-well potential.

Prediction of piezoelectric properties

Motivated by the above results, we performed total-energy calculations as a function of Cu displacements at various c -lattice parameters. We changed the c parameter by the corresponding amount, held the other lattice parameters constant and allowed the atoms to move. As estimated by Poisson ratios of other layered materials^{23,24} between 0.1 and 0.3, we found negligible structural, energy and polarization changes. It was found that most of the compression manifests itself in a reduction of the vdW gap, while the layer thickness changes only slightly. From these structures, we calculate the energy curves, ion–ion distances, polarization and mechanical stress.

It can be seen that the local energy minima of the +LP state vanish for smaller c -lattice parameters whereas the local energy minima of the +HP state vanish for larger c -lattice parameters, as shown in Fig. 1d (see also Supplementary Fig. 3a,b), which shows only the positive polarization states for symmetry reasons. This result demonstrates that the quadruple well is tunable by strain and can become a double well. As a result, the polarization values are also dependent on c -lattice parameter (Supplementary Fig. 3c,d). A key prediction of the theory, therefore, is the fact that, though the energy barrier between the LP and HP phases is smaller than the thermal energy, $k_B T$ (the Boltzmann constant multiplied by temperature) at room temperature, both phases can be stabilized by varying c -lattice parameters.

In Fig. 1e,f, we show the polarization as a function of stress for each of the positive polarization states for the two phases around their respective equilibrium lattice constant, which is characterized by zero stress. From these data, we can extract the longitudinal piezoelectric coefficients as follows.

The third-rank piezoelectric tensor, d_{kij} , can be defined through the displacement field vector $\mathbf{D}_i = \epsilon_0 \mathbf{E}_i + \mathbf{P}_i$, where \mathbf{E}_i is the electric field vector, \mathbf{P}_i the polarization vector and ϵ_0 is the vacuum permittivity²⁵:

$$d_{kij} = \left(\frac{\partial \mathbf{D}_k}{\partial T_{ij}} \right) \Big|_{\mathbf{E}} = \left(\frac{\partial \mathbf{P}_k}{\partial T_{ij}} \right) \Big|_{\mathbf{E}=0} \quad (1)$$

where T_{ij} is the second-rank stress tensor. Thus, linear fits to the calculated points in Fig. 1e can be used to obtain values for the

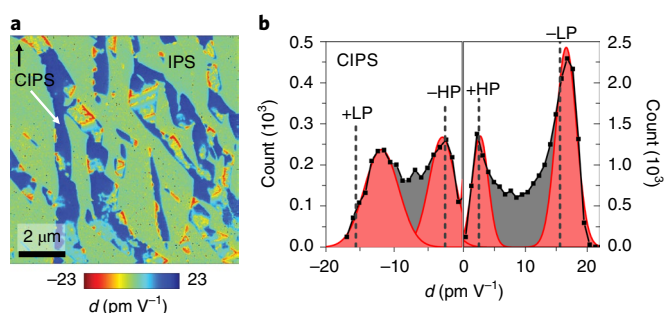


Fig. 2 | Piezoelectric constant experimentally quantified from PFM.

a, Quantified piezoelectric constant map as measured by PFM at room temperature. The colour scale depicts the magnitude and direction of the measured piezoresponse. **b**, Histogram of the measured values of the CIPS phase with Gaussian function fits around the four distinct maxima. Dotted lines depict the theoretically predicted values of the four polarization states.

longitudinal piezoelectric coefficients d_{333} of the two positive polarization states. We find that, near the equilibrium c -lattice parameter value, the +LP state has a large negative piezoelectric coefficient, $d_{333} = -15.6 \pm 0.6 \text{ pm V}^{-1}$, while the +HP state has a relatively small positive piezoelectric constant, $2.5 \pm 0.7 \text{ pm V}^{-1}$. The negative sign of the piezoelectric coefficient for the +LP state agrees with previous work^{8,13}, where evidence for a negative piezoelectric coefficient was found. The piezoelectric and ferroelectric properties of the high-polarization state are reported in this study.

The atomistic origin of the negative sign of the piezoresponse in the +LP state can be traced to the high degree of anharmonicity in the quadruple-well potential as a function of Cu displacements, which underlies the response of the potential minima to strain. In particular, we find that compression of the lattice along the inter-layer stacking direction leads to an increased displacement of Cu away from the In site. As a result, the spontaneous polarization increases with pressure, as reflected in Fig. 1e for small negative stresses, resulting in net negative longitudinal piezoresponse. In contrast, the +HP state behaves in the conventional way, exhibiting decreased Cu displacement under compression of the lattice, as reflected in Fig. 1f, and thus positive piezoresponse. The strain dependence of the second minimum (+HP state) is relatively small, however, leading to a small piezoelectric constant. We can attribute this result to the fact that positive strain weakens the Cu–S interaction across the vdW gap (longer bond length), which is expected to lead to lower polarization, while the increased Cu–In distance would be expected to result in larger moments and higher polarization. The net effect is a near-constant polarization magnitude for this high-polarization regime.

Experimental verification of piezoelectric constants

In the following, we provide direct evidence for the existence of all four polarization states using PFM, as described in detail in Methods^{26,27}. The piezoelectric constant can be expressed through the change in strain, S_{ij} , as function of electric field (equation (2)). PFM measures the dynamic surface displacement ΔL as function of applied voltage, ΔV , typically along the normal of the surface (out-of-plane). Extracting the piezoelectric tensor components from the PFM signal is very complex, due to the capability to probe only surface displacement but not 3D volume changes, and the signal can be affected by strain, radial field distribution around the biased tip or mechanical clamping^{28,29}. PFM is often described as probing the effective longitudinal piezoelectric constant, which is extracted through $d = \Delta L / \Delta V$. It has been shown that in some systems this is

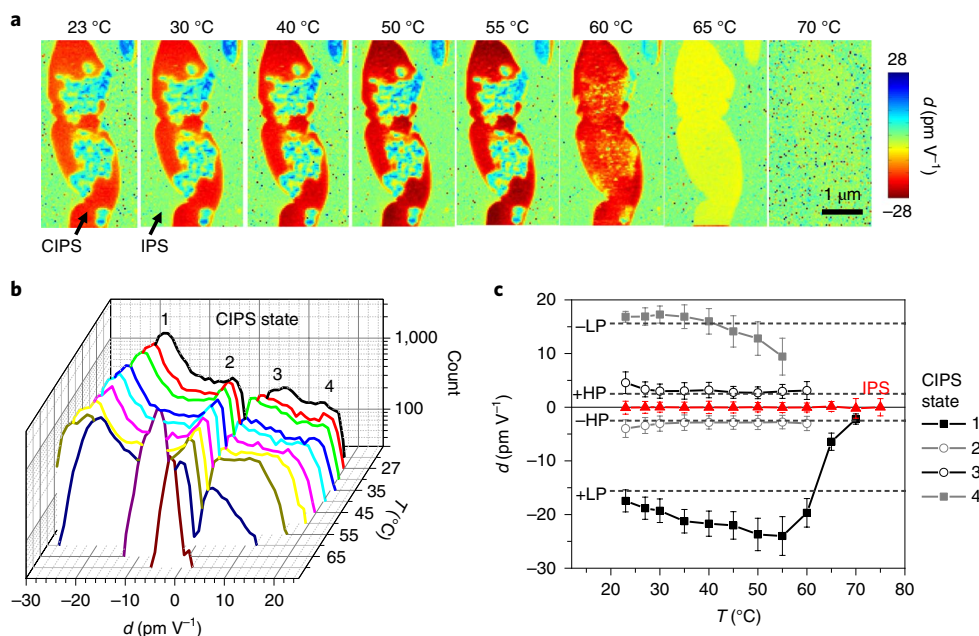


Fig. 3 | Temperature-dependent polarization-state distribution as measured by PFM. a, Temperature-dependent PFM measurements between room temperature and 70 °C across Curie temperature selected from a $10 \times 10 \mu\text{m}^2$ area (Supplementary Fig. 5). **b**, Histograms of measured piezoelectric response analysed for CIPS only. **c**, Temperature-dependent piezoelectric constant extracted for four distinct states, with theoretical piezoelectric constant for comparison. The data points are the position of the histogram peaks for each phase, and error bars correspond to peak widths.

closely aligned with the piezoelectric tensor component along the probed crystallographic axis^{30,31}:

$$d_{kij} = \left(\frac{\partial S_{ij}}{\partial E_k} \right) \Big|_T \quad (2)$$

Here, PFM probes the effective longitudinal piezoelectric constant, d , which is most closely aligned with d_{333} since the probed surface displacement and the main component of the applied electric field are aligned with the z direction of CIPS.

We performed PFM experiments between room temperature and 70 °C on phase-separated, CIPS and $\text{In}_{4/3}\text{P}_2\text{S}_6$ (IPS) phases³². IPS is Cu-free and non-ferroelectric, and allows us to account for non-ferroelectric signal contribution to the local measurements of piezoelectric response. The PFM responses from CIPS and IPS were analysed separately after a masking procedure (Supplementary Fig. 4). The PFM image at room temperature (Fig. 2a) shows strong piezoresponse from ferroelectric CIPS and near-zero signal from the non-ferroelectric IPS phase. Furthermore, the histogram of the piezoresponse on the CIPS phase (Fig. 2b) shows four distinct maxima that align well with the theoretically predicted values, and are described by Gaussian functions (red areas). The positions of the peaks represent the average values while the widths correspond to error bars. The information provided by DFT about signage and magnitude of the piezoelectric constants of the LP and HP phases is used to uniquely assign all four polarization states to the observed PFM contrast levels. We identify the pair $16.6 \pm 0.8 \text{ pm V}^{-1}$ and $-11.8 \pm 1.3 \text{ pm V}^{-1}$ as corresponding to the positive and negative polarization states, respectively, of the LP phase, with a theoretical value of $\pm 15.6 \text{ pm V}^{-1}$. The pair 2.7 ± 0.7 and $2.9 \pm 1.0 \text{ pm V}^{-1}$ is assigned to the negative and positive polarization states of the HP phase, respectively, in excellent agreement with the theoretical absolute value of $\pm 2.5 \text{ pm V}^{-1}$. Based on the very small energy barrier between the HP and LP phases, which is below the thermal energy at room temperature, the observation of spatially separated LP and HP phases by PFM can be explained only by local strain stabilization—

that is, local variations in c -lattice parameter—which confirms our theoretical prediction based on Fig. 1d. The local strain distribution is assumed to be dependent on sample history and synthesis conditions, as well as the number of defects. Therefore, estimation of the ratio of the LP and HP phases using a Maxwell–Boltzmann distribution is not appropriate.

Temperature-induced transition between polarization states

Having assigned the observed polarization states accordingly, we are now able to observe the evolution of all polarization states toward the Curie temperature, T_c , on the local scale using temperature-dependent PFM measurements (Fig. 3a and Supplementary Fig. 5). From a statistical analysis of the images (Fig. 3b), we derived the temperature dependence of the d values of the four polarization states and plotted their trajectories (Fig. 3c). The IPS phase is used as reference and changes little with temperature, confirming the absence of non-piezoelectric signal origins (see also Supplementary Fig. 6a). From room temperature to 55 °C, all four polarization states exist. At 60 °C, the number of polarization states is reduced to three as the $-LP$ state disappears. Further increase in temperature to 65 °C reduces the number of polarization states to one, before the piezoelectric constant of CIPS is indistinguishable from IPS above the Curie temperature. Interconversion of the states prevents direct measurement of the Curie temperature for high-polarization states, but interconversion per se could be useful in the context of applications—for example, in utilizing pyroelectric or electrocaloric responses. As predicted by DFT, ferroelectric properties are very strain sensitive as evident from PFM images acquired under different mechanical pressure (see Extended data Fig. 1 and Supplementary Fig. 7).

Field-induced transition between polarization states

Finally, we demonstrate polarization switching under electric fields using switching spectroscopy²⁷. For the experimental study, we selected two areas based on the map of piezoelectric constant (Fig. 4a) and performed 3×3 -point grids in the large negative–

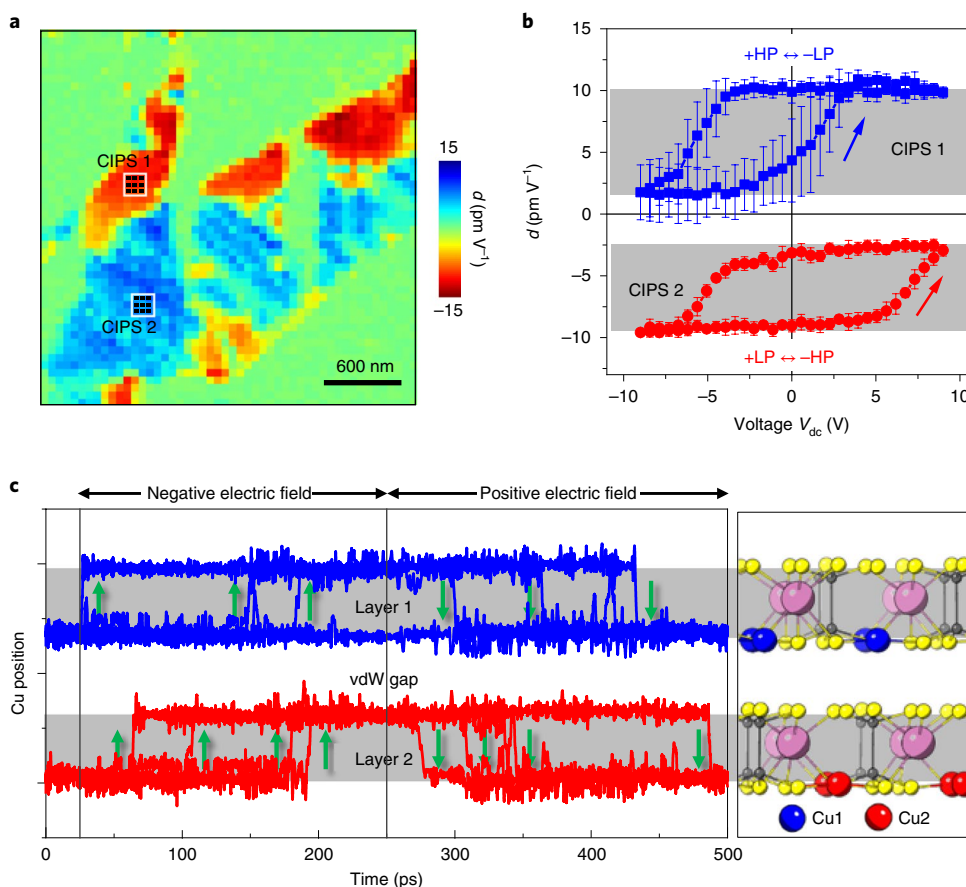


Fig. 4 | Bias-induced polarization switching. **a**, Map of piezoelectric constant in a $3 \times 3 \mu\text{m}^2$ area, with areas of interest highlighted. **b**, Piezoelectric hysteresis loop as function of d.c. bias V_{dc} averaged over a 3×3 -point grid within the two domains (CIPS 1 and CIPS 2) in the ferroelectric CIPS phase, as measured by PFM. The data points are the mean of the response, the error bars correspond to s.d. **c**, Reversible Cu displacements obtained by quantum molecular dynamics simulations. Displacements are shown for the four Cu atoms in each of the two middle layers of a four-layer CIPS sample initially under a negative electric field, which is switched to positive at 250 ps. The Cu atoms in the top and bottom layers are coloured blue and red, respectively. The structure of CIPS is shown in reference to the Cu position.

positive piezoelectric constant (CIPS 1, +LP) and small positive piezoelectric constant (CIPS 2, +HP) regions, as indicated in Fig. 4a. The two distinct polarization domains show different switching pathways (Fig. 4b). In both domains the ferroelectric hysteresis is reversibly changing between two polarization states, depicted by small and large piezoelectric response levels of the same sign. Based on relative amplitude and sign of the bias-dependent change in piezoelectric response, we can assign the associated polarization phase. In the first area (CIPS 1), polarization switches from the +HP to the -LP state under positive voltages applied to the tip (negative fields). In contrast to this, the second area (CIPS 2) shows stable switching from +LP to -HP under positive voltages. These results demonstrate that polarization is reversible, and that bias can be used to cross between the LP and HP phases. This means that all four potential-energy minima can be accessed by electric field, and that the ferroelectric switching of the HP state involves the LP state. Therefore, the HP phase cannot be viewed as an independent double-well potential ferroelectric phase, which makes CIPS a quadruple-well ferroelectric rather than two double-well ferroelectrics. Symmetric polarization loops observed on capacitors of CIPS, and in other PFM studies^{8,12,13}, can be explained by switching involving only LP or only HP states. The possibility of polarization switching is further demonstrated by performing quantum molecular dynamics simulations under electric field, and tracking the Cu positions of two individual layers from the centre of a four-layer stack to

avoid the influence of free surfaces (Fig. 4c). Each layer contains four Cu atoms that are tracked. In the top layer (blue), one Cu atom switches immediately to the other side of the layer followed by multiple switching events. At the point of field reversal at 250 ps, three out of four Cu atoms have switched. In the bottom layer (red), all four Cu atoms switch under negative electric fields. Following field reversal, all Cu atoms switch back to the bottom side of the layer. We note that the Cu atoms switch independently from each other and even partially back-switch. Both experiment and theory suggest that complex switching mechanisms are a subject suitable for further studies.

Outlook

Through a combination of first-principles calculations and local electromechanical material characterization, we have demonstrated the existence of a quadruple-well potential for uniaxial Cu-ion displacements in layered CuInP_2S_6 . This feature is a direct consequence of the ability of Cu atoms to move into the vdW gap of the material, resulting in two distinct polarization phases. The first phase features Cu atoms within the layer, has low polarization and is very sensitive to strain, resulting in a negative longitudinal piezoelectric coefficient. In the second phase, Cu atoms move partially into the vdW gap and bond with S atoms across the gap, doubling the polarization value and featuring a small positive longitudinal piezoelectric coefficient. The difference in piezoresponse

enables the direct detection of the two phases at the local scale. Indeed, we have experimentally observed the coexistence of all four polarization states, as well as their individual temperature- and pressure-dependent interconversions. Polarization switching has been demonstrated both experimentally and in theory, and shows complex, bias-induced transformations between the individual polarization states. The rich spectrum of polarization states in CIPS, as well as the ability to manipulate them with temperature, pressure and bias, opens the pathway to controlling and utilizing these states—for example, in the context of electrocaloric and pyroelectric applications. The realization of uniaxial multi-well potential in the vdW solid, as presented here, is a different mechanism, complementary to multi-axial ferroelectrics^{33,34} and triple-well ferroelectrics with one zero-polarization state^{35,36}. In sum, CIPS can be viewed as bridging the properties of ferroelectrics—distinct polarization states, and those of ionic conductors—multiple potential minima for ionic displacements separated by relatively shallow potential barriers, enabled by the accommodating vdW gap bonding between individual layers. The concomitantly more complex ferroelectric properties suggest equally complex pyroelectric, electrocaloric and thermal material behaviours for prospective applications in computing and energy conversion. The importance of chemical interactions across the vdW gap, on the other hand, necessitates reconsideration of the mechanisms behind size effects in this material and related thiophosphates, and possibly enables new approaches to the tuning and enhancing of proximate coupling between ferroelectric and electronic properties in a vdW heterostructure.

Online content

Any methods, additional references, Nature Research reporting summaries, source data, extended data, supplementary information, acknowledgements, peer review information; details of author contributions and competing interests; and statements of data and code availability are available at <https://doi.org/10.1038/s41563-019-0532-z>.

Received: 25 January 2019; Accepted: 8 October 2019;
Published online: 18 November 2019

References

- Susner, M. A., Chyasnachyus, M., McGuire, M. A., Ganesh, P. & Maksymovych, P. Metal thio- and selenophosphates as multifunctional van der Waals layered materials. *Adv. Mater.* **29**, 1602852 (2017).
- Park, J. G. Opportunities and challenges of 2D magnetic van der Waals materials: magnetic graphene? *J. Phys. Condens. Matter* **28**, 301001 (2016).
- Du, K. Z. et al. Weak van der Waals stacking, wide-tange band gap, and Raman study on ultrathin layers of metal phosphorus trichalcogenides. *ACS Nano* **10**, 1738–1743 (2016).
- Maisonneuve, V. et al. Ionic conductivity in ferroic CuInP_2S_6 and CuCrP_2S_6 . *Ferroelectrics* **196**, 577–580 (1997).
- Balke, N. et al. Locally controlled Cu-ion transport in layered ferroelectric CuInP_2S_6 . *ACS Appl. Mater. Interfaces* **10**, 27188–27194 (2018).
- Dietrich, C. et al. Local structural investigations, defect formation, and ionic conductivity of the lithium ionic conductor $\text{Li}_4\text{P}_2\text{S}_6$. *Chem. Mater.* **28**, 8764–8773 (2016).
- Morozovska, A. N., Eliseev, E. A., Morozovsky, N. V. & Kalinin, S. V. Ferroionic states in ferroelectric thin films. *Phys. Rev. B* **95**, 195413 (2017).
- Liu, F. et al. Room-temperature ferroelectricity in CuInP_2S_6 ultrathin flakes. *Nat. Commun.* **7**, 12357 (2016).
- Maisonneuve, V., Cajipe, V., Simon, A., Von Der Muhll, R. & Ravez, J. Ferroelectric ordering in lamellar CuInP_2S_6 . *Phys. Rev. B* **56**, 10860–10868 (1997).
- Simon, A., Ravez, J., Maisonneuve, V., Payen, C. & Cajipe, V. B. Paraelectric ferroelectric transition in the lamellar thiophosphate CuInP_2S_6 . *Chem. Mater.* **6**, 1575–1580 (1994).
- Bourdon, X., Grimmer, A. R. & Cajipe, V. B. P-31 MAS NMR study of the ferrielectric-paraelectric transition in layered CuInP_2S_6 . *Chem. Mater.* **11**, 2680–2686 (1999).
- Si, M. et al. Room-temperature electrocaloric effect in layered ferroelectric CuInP_2S_6 for solid-state refrigeration. *ACS Nano* **13**, 8760–8765 (2019).
- Neumayer, S. M. et al. Giant negative electrostriction and dielectric tunability in a van der Waals layered ferroelectric. *Phys. Rev. Mater.* **3**, 024401 (2019).
- You, L. et al. Origin of giant negative piezoelectricity in a layered van der Waals ferroelectric. *Sci. Adv.* **5**, eaav3780 (2019).
- Katsouras, I. et al. The negative piezoelectric effect of the ferroelectric polymer poly(vinylidene fluoride). *Nat. Mater.* **15**, 78–84 (2016).
- Liu, S. & Cohen, R. E. Origin of negative longitudinal piezoelectric effect. *Phys. Rev. Lett.* **119**, 207601 (2017).
- Bernardini, F., Fiorentini, V. & Vanderbilt, D. Spontaneous polarization and piezoelectric constants of III–V nitrides. *Phys. Rev. B* **56**, 10024–10027 (1997).
- Shimada, K., Sota, T., Suzuki, K. & Okumura, H. First-principles study on piezoelectric constants in strained BN, AlN, and GaN. *Jpn. J. Appl. Phys.* **37**, L1421–L1423 (1998).
- Ondrejko, P., Marton, P., Guennou, M., Setter, N. & Hlinka, J. Piezoelectric properties of twinned ferroelectric perovskites with head-to-head and tail-to-tail domain walls. *Phys. Rev. B* **88**, 024114 (2013).
- Song, W. S., Fei, R. X. & Yang, L. Off-plane polarization ordering in metal chalcogen diphosphates from bulk to monolayer. *Phys. Rev. B* **96**, 235420 (2017).
- Stengel, M. & Iniguez, J. Electrical phase diagram of bulk BiFeO_3 . *Phys. Rev. B* **92**, 235148 (2015).
- Sharma, P. et al. Morphotropic phase elasticity of strained BiFeO_3 . *Adv. Mater. Interfaces* **3**, 1600033 (2016).
- Liu, K. et al. Elastic properties of chemical-vapor-deposited monolayer MoS_2 , WS_2 , and their bilayer heterostructures. *Nano. Lett.* **14**, 5097–5103 (2014).
- Woo, S., Park, H. C. & Son, Y. W. Poisson's ratio in layered two-dimensional crystals. *Phys. Rev. B* **93**, 075420 (2016).
- Lines M. E. & Glass A. M. *Principles and Applications of Ferroelectrics and Related Materials* (Oxford Univ. Press, 1977).
- Gruverman, A., Auciello, O. & Tokumoto, H. Scanning force microscopy for the study of domain structure in ferroelectric thin films. *J. Vac. Sci. Technol. B* **14**, 602–605 (1996).
- Jesse, S., Baddorf, A. P. & Kalinin, S. V. Switching spectroscopy piezoresponse force microscopy of ferroelectric materials. *Appl. Phys. Lett.* **88**, 062908 (2006).
- Eliseev, E. A., Kalinin, S. V., Jesse, S., Bravina, S. L. & Morozovska, A. N. Electromechanical detection in scanning probe microscopy: tip models and materials contrast. *J. Appl. Phys.* **102**, 014109 (2007).
- Setter, N. et al. Ferroelectric thin films: review of materials, properties, and applications. *J. Appl. Phys.* **100**, 051606 (2006).
- Jungk, T., Hoffmann, A. & Soergel, E. Quantitative analysis of ferroelectric domain imaging with piezoresponse force microscopy. *Appl. Phys. Lett.* **89**, 163507(1)–163507(3) (2006).
- Balke, N. et al. Quantification of surface displacements and electromechanical phenomena via dynamic atomic force microscopy. *Nanotechnology* **27**, 425707 (2016).
- Susner, M. A. et al. High- T_c layered ferrielectric crystals by coherent spinodal decomposition. *ACS Nano* **9**, 12365–12373 (2015).
- Zavaliche, F. et al. Multiferroic BiFeO_3 films: domain structure and polarization dynamics. *Phase Transit.* **79**, 991–1017 (2006).
- Baudry, L., Lukyanchuk, I. & Vinokur, V. M. Ferroelectric symmetry-protected multibit memory cell. *Sci. Rep.* **7**, 42196 (2017).
- Dieguez, O. & Vanderbilt, D. Theoretical study of ferroelectric potassium nitrate. *Phys. Rev. B* **76**, 134101 (2007).
- Yevych, R. M. & Vysochanskii, Y. M. Triple well potential and macroscopic properties of $\text{Sn}_2\text{P}_2\text{S}_6$ ferroelectrics near phase transition. *Ferroelectrics* **412**, 38–44 (2011).
- Momma, K. & Izumi, F. VESTA 3 for three-dimensional visualization of crystal, volumetric and morphology data. *J. Appl. Crystallogr.* **44**, 1272–1276 (2011).

Publisher's note Springer Nature remains neutral with regard to jurisdictional claims in published maps and institutional affiliations.

This is a U.S. government work and not under copyright protection in the U.S.; foreign copyright protection may apply 2019

Methods

Calculations. Below the Curie temperature, CIPS has a monoclinic structure (space group, Cc) consisting of four formula units per unit cell, with cell parameters $a = 6.096 \text{ \AA}$, $b = 10.565 \text{ \AA}$, $c = 13.187 \text{ \AA}$ and $\beta = 99.12^\circ$ (note that Maisonneuve et al.³⁸ use a non-standard but equivalent setting for this cell)^{38,39}. We find that relaxation calculations using the DFT-D3 (Becke–Johnson) vdW formulation, as developed by Grimme and colleagues^{40,41}, accurately reproduce these lattice parameters, with the differences being 0.32, 0.22, -0.72 and -0.01% for a , b , c and β , respectively. The absolute lattice parameters are 6.12 \AA for a , 10.59 \AA for b and 13.09 \AA for c .

The DFT calculations in this study used both the ABINIT v.8.2.3 computational package⁴² and the Vienna ab initio Simulation Package (VASP)⁴³ with the projected-augmented wave (PAW) method^{44,45}, and were carried out under the Perdew–Burke–Ernzerhof generalized gradient approximation. We considered two versions of vdW exchange–correlation functionals: the DFT-D2 method and the DFT-D3 (Becke–Johnson (BJ)) method^{40,41,46}. For the ABINIT calculations, the atoms are modelled by norm-conserving optimized pseudo-potentials⁴⁷ generated using OPIUM (<http://opium.sourceforge.net>), and all are further refined using the designed non-local methodology⁴⁸. We pseudize the following orbitals: $3s$, $3p$ and $3d$ for S; $3s$, $3p$ and $3d$ for P; $3d$, $4s$ and $4p$ for Cu; and $4s$, $4p$, $4d$, $5s$ and $5p$ for In. VASP calculations use the as-supplied PAW potentials. All calculations use a Monkhorst–Pack k-point grid⁴⁹ of $4 \times 4 \times 4$. For relaxation calculations, the system is considered to be relaxed when successive self-consistent iterations yield total-energy differences $< 5 \times 10^{-7}$ eV per unit cell and atomic forces $< 5 \times 10^{-4}$ eV \AA^{-1} . Energy cut-offs for the pseudo-potentials and the structural and electronic calculations are 680 eV. Polarization and phonon-frequency calculations are also carried out using pertinent routines in ABINIT.

Using ABINIT, we find that the DFT-D3(BJ) vdW interaction reproduces the experimentally determined cell parameters of CIPS^{38,39} better than the DFT-D2 method: parameters a , b , c and β have errors of 0.32, 0.22, -0.72 and -0.01% , respectively, for the DFT-D3(BJ) method, while for DFT-D2 the corresponding values are 0.57, 0.44, 1.23 and -0.51% . Comparison of the lattice constants under the PAW method within VASP using the DFT-D3 and DFT-D3(BJ) vdW interactions is discussed in the Supplementary information, again indicating the favourability of the DFT-D3(BJ) vdW method.

The bias-induced ferroelectric switching process is simulated using quantum molecular dynamics simulations and a (2×1) model containing four layers of CuInP_2S_6 with a vacuum separation of 25 \AA in the z direction. Under these boundary conditions, the layer spacing of CIPS is not fixed. There are fluctuations in the interlayer distance, while the lattice parameters a and b do not change during the switching process. The Brillouin zone is sampled only at the Γ point. For quantum molecular dynamics simulations, a canonical (NVT) ensemble was used^{50,51} within the VASP⁴³, and a plane wave-basis cut-off energy of 400 eV. The time interval between steps was 10 fs. An external electric field was applied using the methods of Neugebauer and Scheffler⁵² and Makov and Payne⁵³. Initially, the system was simulated below the Curie temperature at -173.15°C (100 K) for 25 ps to obtain equilibration conditions. For ferroelectric switching, an electric field was applied along the z direction ($E = 1.5 \text{ eV \AA}^{-1}$) for 225 ps, and then the direction of the electric field was reversed for 250 ps. The switching was simulated at the higher temperature of -73.15°C (200 K) for switching events to occur within the observed time frame. See also Supplementary Fig. 8 for more information.

Material synthesis. Details about the material synthesis can be found elsewhere¹. Measurements were performed on heterostructured crystals of several micrometres in thickness, comprising CIPS and IPS phases³². The average composition of the crystal was $\text{Cu}_{0.4}\text{In}_{1.2}\text{P}_2\text{S}_6$.

Experimental. Piezoresponse force microscopy was carried out using a Bruker Icon atomic force microscope in air. A temperature-stage was used to perform PFM as a function of temperature. For each temperature step, the sample was equilibrated for 10 min before measurement. For each temperature the same area was found based on topographic features, to account for drift. Pressure-dependent PFM images were obtained in the controlled environment of an argon-filled glovebox, with water and oxygen levels < 0.1 ppm. All alternating current voltages for PFM measurements were 1 V_{ac} . The cantilever used for all studies was a Nanosensor PPP-EFM with a typical free resonance of 75 kHz and a typical force constant of 3 N m^{-1} . Samples mounted on a silver-paint support were cleaved shortly before microscopy experiments. PFM imaging was performed using band excitation techniques, and ferroelectric hysteresis was probed using switching spectroscopy²⁷. All ferroelectric hystereses shown depict off-field hysteresis probing the piezoelectric response after the switching pulses. PFM amplitude was quantified using the cantilever sensitivity. We tested the requirement for additional amplitude correction factors based on cantilever mode shapes, as described by Balke et al.³¹, but the test revealed an error of $< 4\%$ when using only the cantilever sensitivity for quantification. The PFM phase was corrected for instrumental phase offsets and correlation between measured electromechanical response and the sign of piezoelectric coefficients. Measurement artefacts, such as electrostatic signal contributions, were ruled out by confirming a near-zero PFM response on the non-ferroelectric IPS phase of the sample. The PFM response was analysed separately for the ferroelectric CIPS and non-ferroelectric IPS phases.

Data availability

The experimental and theoretical data presented in this work are available from the corresponding authors upon reasonable request.

References

- Maisonneuve, V., Evain, M., Payen, C., Cajipe, V. B. & Molinie, P. Room-temperature crystal-structure of the layered phase $\text{Cu}(\text{I})\text{In}(\text{III})\text{P}_2\text{S}_6$. *J. Alloy. Compd.* **218**, 157–164 (1995).
- Belsky, A., Hellenbrandt, M., Karen, V. L. & Luksch, P. New developments in the Inorganic Crystal Structure Database (ICSD): accessibility in support of materials research and design. *Acta Crystallogr. B* **58**, 364–369 (2002).
- Grimme, S., Antony, J., Ehrlich, S. & Krieg, H. A consistent and accurate ab initio parametrization of density functional dispersion correction (DFT-D) for the 94 elements H–Pu. *J. Chem. Phys.* **132**, 154104 (2010).
- Grimme, S., Ehrlich, S. & Goerigk, L. Effect of the damping function in dispersion corrected density functional theory. *J. Comput. Chem.* **32**, 1456–1465 (2011).
- Gonze, X. et al. First-principles computation of material properties: the ABINIT software project. *Comput. Mater. Sci.* **25**, 478–492 (2002).
- Kresse, G. & Furthmüller, J. Efficient iterative schemes for ab initio total-energy calculations using a plane-wave basis set. *Phys. Rev. B* **54**, 11169–11186 (1996).
- Blöchl, P. E. Projector augmented-wave method. *Phys. Rev. B* **50**, 17953–17979 (1994).
- Kresse, G. & Joubert, D. From ultrasoft pseudopotentials to the projector augmented-wave method. *Phys. Rev. B* **59**, 1758–1775 (1999).
- Grimme, S. Semiempirical GGA-type density functional constructed with a long-range dispersion correction. *J. Comput. Chem.* **27**, 1787–1799 (2006).
- Rappe, A. M., Rabe, K. M., Kaxiras, E. & Joannopoulos, J. D. Optimized pseudopotentials. *Phys. Rev. B* **41**, 1227–1230 (1990).
- Ramer, N. J. & Rappe, A. M. Designed nonlocal pseudopotentials for enhanced transferability. *Phys. Rev. B* **59**, 12471–12478 (1999).
- Monkhorst, H. J. & Pack, J. D. Special points for Brillouin-zone integrations. *Phys. Rev. B* **13**, 5188–5192 (1976).
- Kresse, G. & Hafner, J. *Ab initio* molecular dynamics for open-shell transition metals. *Phys. Rev. B* **48**, 13115–13118 (1993).
- Kresse, G. & Hafner, J. *Ab initio* molecular-dynamics simulation of the liquid-metal–amorphous-semiconductor transition in germanium. *Phys. Rev. B* **49**, 14251–14269 (1994).
- Neugebauer, J. & Scheffler, M. Adsorbate-substrate and adsorbate-adsorbate interactions of Na and K adlayers on $\text{Al}(111)$. *Phys. Rev. B* **46**, 16067–16080 (1992).
- Makov, G. & Payne, M. C. Periodic boundary conditions in ab initio calculations. *Phys. Rev. B* **51**, 4014–4022 (1995).

Acknowledgements

The experimental work, including part of the data analysis and interpretation, was supported by the US Department of Energy, Office of Science, Basic Energy Sciences, Materials Science and Engineering Division. Theory was supported by the US Department of Energy (grant no. DE-FG02-09ER46554) and by the McMinn Endowment at Vanderbilt University. The experiments were conducted at the Center for Nanophase Materials Sciences, which is a DOE Office of Science User Facility that also provided support with data collection and interpretation. Partial support for sample synthesis, experiments and theory was provided by the Laboratory Directed Research and Development program at the Oak Ridge National Laboratory. Calculations were performed at the National Energy Research Scientific Computing Center, a DOE Office of Science User Facility supported by the Office of Science of the US Department of Energy under contract no. DE-AC02-05CH11231. Manuscript preparation was partially funded by the Air Force Research Laboratory under an Air Force Office of Scientific Research grant (LRIR grant no. 14RQ08COR) and a grant from the National Research Council.

Author contributions

J.A.B., L.T., A.O. and S.T.P. performed the DFT calculations. S.M.N., M.C., P.M. and N.B. designed and performed the PFM experiments. M.A.S. and M.A.M. synthesized the samples. S.J. provided data acquisition support. P.G. and S.V.K. provided discussion on theoretical and experimental results. All authors contributed to manuscript writing.

Competing interests

The authors declare no competing interests.

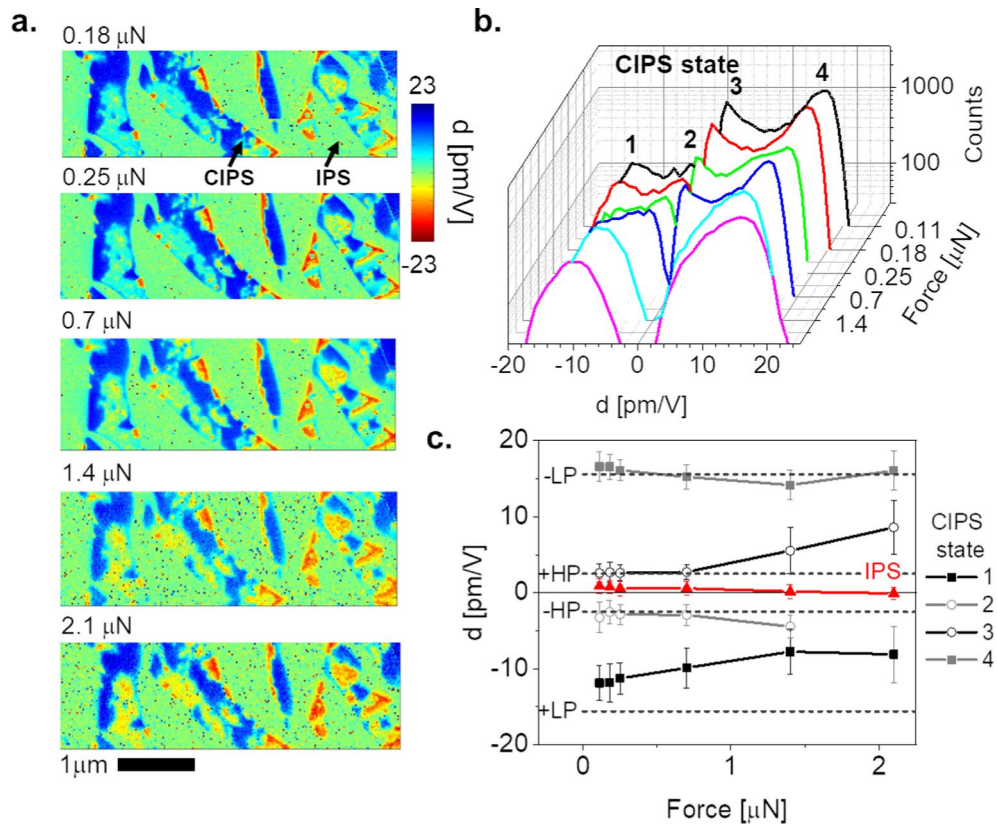
Additional information

Extended data is available for this paper at <https://doi.org/10.1038/s41563-019-0532-z>.

Supplementary information is available for this paper at <https://doi.org/10.1038/s41563-019-0532-z>.

Correspondence and requests for materials should be addressed to S.T.P., P.M. or N.B.

Reprints and permissions information is available at www.nature.com/reprints.



Extended Data Fig. 1 | Pressure-induced polarization switching measured by PFM. (a.) Pressure-dependent PFM measurements from a $10 \times 10 \mu\text{m}^2$ area (Supplementary Fig. 6). (b.) Histograms of measured piezoelectric response of CIPS only. (c.) Pressure-dependent piezoelectric constant extracted for four distinct states and theoretical piezoelectric constant from theory for comparison. Data points are the position of the histogram peaks for each phase and error bars correspond to the peak widths. The d -value is constant or decreasing for LP and increases for HP. The +HP state (light blue) transforms into the -HP state (yellow) indicating a pressure-induced switching event. All changes are reversible. Response on the IPS phase changes little with contact force (see also Supplementary Fig. 7b).